





The Time Delay Distribution and Formation Metallicity of LIGO-Virgo’s Binary Black Holes

Maya Fishbach¹  and Vicky Kalogera 

Center for Interdisciplinary Exploration and Research in Astrophysics (CIERA) and Department of Physics and Astronomy, Northwestern University, 1800 Sherman Avenue, Evanston, IL 60201, USA

Received 2021 May 13; revised 2021 May 26; accepted 2021 May 26; published 2021 June 17

Abstract

We derive the first constraints on the time delay distribution of binary black hole (BBH) mergers using the LIGO-Virgo Gravitational-Wave Transient Catalog. Assuming that the progenitor formation rate follows the star formation rate (SFR), the data favor that 43%–100% of mergers have delay times < 4.5 Gyr (90% credibility). Adopting a model for the metallicity evolution, we derive joint constraints for the metallicity-dependence of the BBH formation efficiency and the distribution of time delays between formation and merger. Short time delays are favored regardless of the assumed metallicity dependence, although the preference for short delays weakens as we consider stricter low-metallicity thresholds for BBH formation. For a $p(\tau) \propto \tau^{-1}$ time delay distribution and a progenitor formation rate that follows the SFR without metallicity dependence, we find that $\tau_{\min} < 2.2$ Gyr, whereas considering only the low-metallicity $Z < 0.3 Z_{\odot}$ SFR, $\tau_{\min} < 3.0$ Gyr (90% credibility). Alternatively, if we assume long time delays, the progenitor formation rate must peak at higher redshifts than the SFR. For example, for a $p(\tau) \propto \tau^{-1}$ time delay distribution with $\tau_{\min} = 4$ Gyr, the inferred progenitor rate peaks at $z > 3.9$ (90% credibility). Finally, we explore whether the inferred formation rate and time delay distribution vary with BBH mass.

Unified Astronomy Thesaurus concepts: [Gravitational waves \(678\)](#); [Gravitational wave astronomy \(675\)](#); [Astrophysical black holes \(98\)](#); [Stellar mass black holes \(1611\)](#); [Cosmological evolution \(336\)](#); [Bayesian statistics \(1900\)](#)

1. Introduction

The latest catalog of compact binary coalescences observed by Advanced LIGO (LIGO Scientific Collaboration et al. 2015) and Virgo (Acernese et al. 2015), the second Gravitational-Wave Transient Catalog (GWTC-2), includes binary black hole (BBH) mergers out to $z \sim 1$ (Abbott et al. 2021a, 2021b). These observations probe the evolution of the BBH population over the last ~ 8 billion years, providing updated constraints on the merger rate (Abbott et al. 2021b, 2021c) and the mass distribution (Fishbach et al. 2021) as a function of redshift.

Measuring the rate of BBH mergers as a function of redshift yields valuable clues to their evolutionary histories. The BBH merger rate depends on a combination of the progenitor formation rate and the distribution of delay times between formation and merger (Banerjee et al. 2010; O’Shaughnessy et al. 2010; Dominik et al. 2013; Belczynski et al. 2016; Lamberts et al. 2016; Mandel & de Mink 2016; Elbert et al. 2018; Fragione & Kocsis 2018; Kruckow et al. 2018; Rodriguez & Loeb 2018; Chruslinska et al. 2019; Neijssel et al. 2019; du Buisson et al. 2020; Santoliquido et al. 2020; Tang et al. 2020; Santoliquido et al. 2021).

In most formation channels, black holes have a stellar origin, and the progenitor formation rate is closely related to the star formation rate (SFR; Madau & Dickinson 2014; Vangioni et al. 2015; Madau & Fragos 2017; El-Badry et al. 2019). Because the BBH formation efficiency is expected to be a strong function of the stellar metallicity (Kudritzki & Puls 2000; Belczynski et al. 2010; Brott et al. 2011; Fryer et al. 2012), the progenitor formation rate also depends on the metallicity

evolution of the universe (Langer & Norman 2006; Ma et al. 2015; Chruslinska & Nelemans 2019; Chruślińska et al. 2020).

Meanwhile, the time delay between formation and merger is a unique property of the formation channel, and different proposed channels predict different distributions of time delays. Classical isolated binary evolution predicts a power-law time delay distribution $p(\tau) \propto \tau^{\alpha}$, dominated by the gravitational-wave (GW) merger timescale $t \propto a^4$ for an initial orbital separation a (Peters 1964). A typical prediction for the power-law slope is $\alpha = -1$ (O’Shaughnessy et al. 2010; Dominik et al. 2012), assuming a flat-in-log distribution for the initial binary separations $p(a) \propto a^{-1}$ (Abt 1983; Sana et al. 2013), but the exact form of the distribution depends on uncertain physics including stellar winds, mass transfer, and kicks, in addition to the uncertain distribution of orbital separations (O’Shaughnessy et al. 2008, 2010; Mapelli et al. 2017). A subclass of isolated binary evolution, chemically homogeneous evolution predicts longer delay times (Mandel & de Mink 2016; Marchant et al. 2016), with a strong correlation between the formation metallicity and the delay time to merger. At the highest metallicities possible for this channel, $Z \sim 0.2 Z_{\odot}$, the predicted delay times are long, $\tau > 3.5$ Gyr (Mandel & de Mink 2016), whereas at much lower metallicities ($Z \lesssim 0.01 Z_{\odot}$), shorter delay times $\tau < 1$ Gyr are possible (Marchant et al. 2016; du Buisson et al. 2020). Stellar evolution in triple stellar systems, rather than binaries, may also produce BBH mergers, with a time delay distribution skewed toward longer time delays than the isolated binary case, with most delays larger than 1 Gyr (Antonini et al. 2017; Hoang et al. 2018; Rodriguez & Antonini 2018). For BBH formation in young star clusters, most systems experience short delay times, with the predicted delay time distribution peaking at ~ 100 Myr and following a τ^{-1} distribution above 400 Myr (Di Carlo et al. 2020). For dynamically assembled BBHs in

¹ NASA Hubble Fellowship Program Einstein Postdoctoral Fellow.

globular clusters, the delay time distribution depends on the cluster’s virial radius, with larger radii leading to larger delay times (Rodríguez et al. 2018). BBH systems ejected from the cluster prior to merger ($\sim 50\%$ of BBH mergers) are expected to experience very long delay times (with a median of ~ 10 Gyr), while in-cluster mergers occur extremely promptly, which may lead to trends between eccentricity, mass, and spin with merger redshift (Benacquista & Downing 2013; Rodríguez et al. 2016; Banerjee 2017; Rodríguez et al. 2018; Samsing 2018; Kremer et al. 2020; Banerjee 2021). Another proposed site for the dynamical assembly of BBHs is the disks of active galactic nuclei (AGN), which are expected to merge BBHs with short delay times $\tau < 100$ Myr (Yang et al. 2020). However, the BBH merger rate in AGN is expected to peak at relatively low redshifts $z \lesssim 1$ because their formation traces the evolution of the AGN luminosity function (Yang et al. 2020).

Previous work has demonstrated that GW observations can meaningfully constrain the evolution of the merger rate by using a catalog of LIGO-Virgo BBH events at $z \lesssim 1.5$ (Fishbach et al. 2018; Abbott et al. 2019, 2021b; Roulet et al. 2020; Tiwari 2020), combining a BBH catalog with a (non)detection of the astrophysical stochastic background (Callister et al. 2020; Safarzadeh et al. 2020; Abbott et al. 2021c), or anticipating the next generation of ground-based GW detectors, which would trace the evolution of the merger rate across the entire observable universe (Kalogera et al. 2019; Safarzadeh et al. 2019; Vitale et al. 2019; Ng et al. 2021; Romero-Shaw et al. 2020).

In this work, we derive the first observational constraints on the BBH time delay distribution, the progenitor formation rate, and its metallicity dependence. We describe a phenomenological fit to the redshift evolution of the BBH merger rate in Section 2. Fixing the progenitor formation rate to the (low-metallicity) SFR, we derive constraints on the time delay distribution in Section 3. In Section 4, we measure the threshold metallicity for BBH formation and the corresponding progenitor formation rate for fixed time delay distributions. We also explore how the formation rate and time delay may depend on the mass of the BBH system in Section 3.4, and discuss the implications of these findings for BBH formation scenarios in Section 5. Although the GWTC-2 events only probe redshifts $z \lesssim 1$ far below the peak of the SFR at $z \sim 2$, we find that we can already derive useful astrophysical constraints from the observed redshift evolution.

2. BBH Merger Rate as a Function of Redshift

We begin by reviewing the inferred BBH merger rate from GWTC-2. As in Abbott et al. (2021b, 2021c), we jointly fit the mass, spin, and redshift distribution of the BBH population with simple phenomenological models described in the Appendix. The inferred redshift evolution has significant correlations with the mass distribution (Fishbach et al. 2018), and we discuss possible systematic uncertainties associated with the choice of mass model in Section 3.4. In our calculation, we do not take into account the stochastic GW background upper limit reported in Abbott et al. (2021c) because at this stage, it does not provide much additional information compared to the resolved BBH events. Thus, we only consider the merger rate up to $z = 1$. However, like Abbott et al. (2021c), our redshift model allows the merger rate to peak at some redshift z_p , finding that the data disfavor $z_p < 1$.

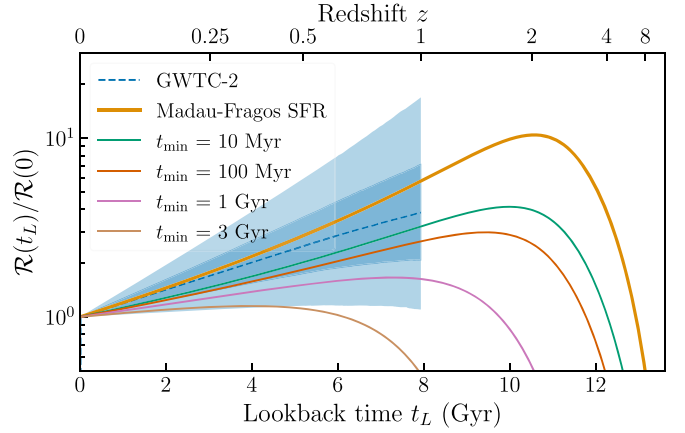


Figure 1. Merger rate as a function of lookback time (or equivalently, redshift) normalized to the merger rate today. In blue, evolution of the merger rate inferred from fitting a population model to the GWTC-2 events. The dashed blue line shows the median, while the shaded bands show 50% and 90% credible intervals. For comparison, the thick gold line shows the Madau–Fragos SFR. The green, orange, pink, and tan lines illustrate predicted merger rate shapes, assuming a formation rate that follows the Madau–Fragos SFR and a τ^{-1} time delay distribution with a minimum time delay of 50 Myr, 100 Myr, 1 Gyr, and 3 Gyr, respectively. If the progenitor formation rate follows the SFR, a distribution of time delays that peaks at long times $\tau \gtrsim 3$ Gyr is in tension with the inferred distribution from GWTC-2.

Figure 1 shows the merger rate evolution $\mathcal{R}(z)$ inferred by fitting the phenomenological $p(m_1, m_2, \chi_{\text{eff}}, z)$ model described in the Appendix to the 44 confident GWTC-2 BBH events analyzed in Abbott et al. (2021b). The blue bands show 50% and 90% symmetric credible regions, while the dashed blue line shows the median. For comparison, we show example merger rate curves for different time delay models that follow $p(\tau) \propto \tau^{-1}$ with different minimum time delays τ_{min} . We assume that the progenitor formation rate follows the Madau & Fragos (2017) SFR. In the following sections, we also consider progenitor formation rates that follow the low-metallicity SFR, for some $Z < Z_{\text{thresh}}$, rather than the total SFR, adopting the mean metallicity–redshift relation from Madau & Fragos (2017). The calculation of the merger rate $\mathcal{R}(z)$ given the progenitor formation rate and the time delay distribution is detailed in the Appendix. From Figure 1, we see that the GWTC-2 measurement of the rate evolution, in reference to the SFR, is informative about the time delay distribution, disfavoring distributions with large $\tau_{\text{min}} \gtrsim 3$ Gyr.

3. Time Delay Inference

The previous section showed a phenomenological fit to the merger rate evolution $\mathcal{R}(z)$. In this section, we adopt a physical parameterization for the redshift evolution by modeling the progenitor formation rate $R_f(z)$ and the time delay distribution $p(\tau)$ (see Equation (A8)). Throughout, we consider maximum time delays of $\tau = 13.5$ Gyr, corresponding to maximum formation redshifts of $z = 14$. Fixing the progenitor formation rate to the SFR, we fit for the time delay distribution under a binned histogram model (Section 3.1) and a power-law model (Section 3.2). We then consider progenitor rates that follow the low-metallicity SFR, and explore how the metallicity-dependence affects the time delay inference (Section 3.3). In Section 3.4 we investigate possible correlations between BBH mass and delay times.

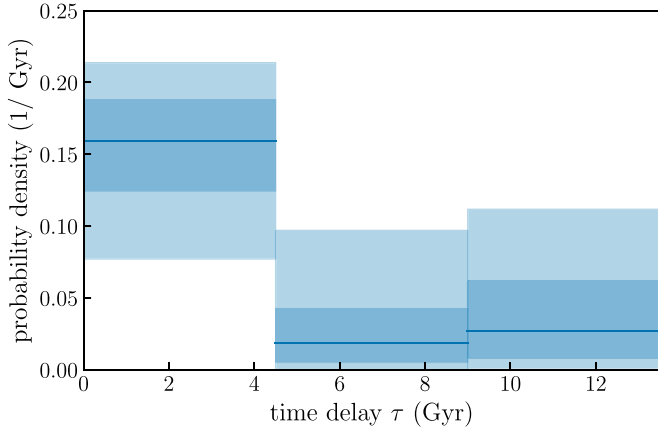


Figure 2. Inferred time delay distribution assuming a binned time delay model for a progenitor rate that follows the SFR. The data are consistent with all BBH systems having time delays smaller than 4.5 Gyr (belonging to the first bin), and requires that at least 43% of mergers experience time delays smaller than 4.5 Gyr.

3.1. Binned Time Delay Model

We begin by modeling the time delay distribution as piecewise constant in n bins with bin edges given by $\{b_i\}_{i=1}^{n+1}$,

$$p(\tau) = \sum_{i=1}^n p_i \Theta(b_i \leq \tau < b_{i+1}), \quad (1)$$

where Θ is an indicator function.

We consider three equally spaced time bins up to $\tau_{\max} = 13.5$ Gyr, fixing the bin edges $b_i = \frac{13.5(i-1)}{3}$ Gyr. We obtain qualitatively similar results when we consider a five-binned model, with larger uncertainties on the bin heights as expected for a model with more free parameters.

As in Section 2, we fit the joint mass–redshift–spin distribution of the BBH population, but we replace the rate evolution model with this physical parameterization. We use priors on the mass and spin parameters as in the Appendix. For the redshift distribution, we choose the Jeffreys prior on the fraction $p_i \times (b_{i+1} - b_i)$ of systems within each time delay bin. The Jeffreys prior for a trinomial distribution is a Dirichlet distribution with concentration parameters $\alpha = 0.5$ (Schafer 1997). We fix the shape of the formation rate $R_f(z)$ to follow the Madau–Fragos SFR.

The inferred time delay distribution $p(\tau)$ is shown in Figure 2. The data are consistent with all mergers belonging to the smallest time delay bin. This is true regardless of the bin boundaries; because the shape of the merger rate evolution is consistent with the SFR, the data are consistent with all BBH mergers having arbitrarily small time delays. The data requires that 43%–100% of delay times are smaller than 4.5 Gyr (90% credibility). While there is a preference for small time delays, this flexible model permits a broad range of time delay distributions. In the following section we explore stricter parameterizations for the time delay distribution.

3.2. Power-law Time Delay Model

In this subsection, we consider a power-law model for the time delay distribution, parameterized by a slope α_τ and a minimum delay time τ_{\min} :

$$p(\tau) \propto \tau^{\alpha_\tau} \Theta(\tau_{\min} \leq \tau < 13.5 \text{ Gyr}). \quad (2)$$

Because the current GW catalog extends only to $z = 1$, we find that the information about the time delay distribution can be summarized by the inferred merger rate at $z = 0$ compared to $z = 1$, or $\mathcal{R}(z = 1) \equiv \mathcal{R}_1$ compared to $\mathcal{R}(z = 0) \equiv \mathcal{R}_0$. Any combination of progenitor formation rate R_f and time delay distribution predicts a value for the ratio $\mathcal{R}_1/\mathcal{R}_0$. We map this quantity onto an effective $(1+z)$ power-law slope parameter κ , taking $\kappa = \ln(\mathcal{R}_1/\mathcal{R}_0)/\ln 2$, and summarize the time delay inference in terms of κ .

Figure 3 shows the effective κ parameter for a family of time delay distributions and progenitor formation rates. In the top left panel (“no Z_{thresh} ”), we fix the formation rate to the SFR and consider power-law time delay distributions characterized by a power-law slope α_τ and a minimum time delay τ_{\min} . Steeper (more negative) power-law slopes imply larger values of κ , as do smaller values of the minimum time delay. We overlay dashed black contours corresponding to the 50% and 90% credible intervals on the merger rate evolution $\mathcal{R}(z)$ inferred from GWTC-2 in Section 2. The model parameter space outside the 90% contour (the hatched region) is ruled out by GWTC-2 at 90% credibility. We can see from the top left panel of Figure 3 that in order to match the inferred redshift evolution between $z = 0$ and $z = 1$, the time delay distribution must be relatively steep ($\alpha_\tau \lesssim -0.5$) and/or peak at a small minimum time delay ($\tau_{\min} \lesssim 3.5$ Gyr).

Fixing the shape of the progenitor formation rate to the SFR (equivalently, fixing Z_{thresh} to be large) and simultaneously fitting for the SFR normalization $R_{f,0}$ and $(\alpha_\tau, \tau_{\min})$ in the power-law time delay model of Equation (2), we obtain the posterior on the distribution of time delays shown in Figure 4. This figure shows the inference on the cumulative distribution function (CDF) of time delays for the posterior (blue) compared to the prior (pink). Under this model, we obtain median delay times $\tau_{50\%} = 2.8^{+3.3}_{-2.6}$ Gyr, compared to the prior $\tau_{50\%} = 6.5^{+3.1}_{-5.6}$ Gyr (90% symmetric credible interval). In the following subsection we will explore how restricting to the low-metallicity SFR affects these results.

3.3. Effect of Metallicity

In this subsection we infer time delay distributions corresponding to progenitor formation rates that follow the low-metallicity SFR, parameterized by a threshold metallicity Z_{thresh} . We assume a default value for the scatter about the mean metallicity–redshift relation of $\sigma_{\log Z} = 0.4$ dex.

We simultaneously vary Z_{thresh} and the time delay distribution in the bottom two panels of Figure 3. The bottom left panel (“ $p(\tau) \propto \tau^{-1}$ time delay”) shows the joint effect of varying Z_{thresh} and τ_{\min} on the merger rate evolution for a τ^{-1} time delay model. The bottom right panel (“log-normal time delay”), instead of a τ^{-1} time delay model, uses a truncated log-normal:

$$p(\tau) \propto \tau^{-1} \exp \left[-\frac{1}{2} \left(\frac{\log_{10} \tau - \log_{10} \mu}{s} \right)^2 \right] \times \Theta(0 \leq \tau < 13.5), \quad (3)$$

with μ shown on the x -axis and s fixed to $s = 0.5$ dex.

As we consider a stricter metallicity cut (smaller Z_{thresh} values) for BBH formation, we move the peak of the progenitor formation rate to higher redshifts, and the data correspondingly allow for larger τ_{\min} or μ to match the observed redshift

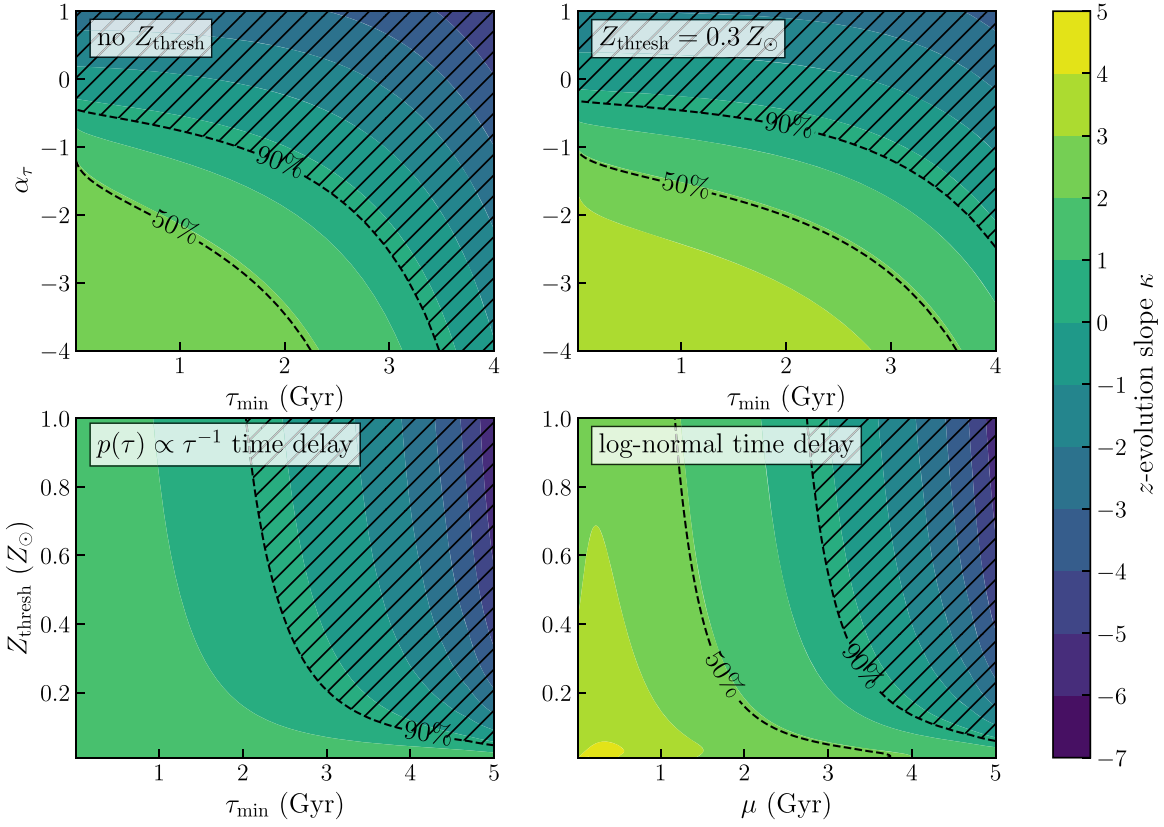


Figure 3. Approximate redshift evolution parameter κ , where $\mathcal{R}(z) = R_0(1+z)^\kappa$ resulting from different time delay and progenitor formation models (filled contours). The dashed black contours denote the 50% and 90% credible bounds on the rate evolution from the GWTC-2 inference, so that the black hatched region of parameter space is excluded at 90% credibility. Top left: the formation rate is assumed to follow the Madau–Fragos SFR, and the time delay distribution follows a power law with variable α_τ and τ_{\min} . Top right: same as the top left panel, but the formation rate is assumed to follow the low-metallicity SFR with $Z_{\text{thresh}} = 0.3 Z_\odot$. We assume a 0.4 dex spread in the mean metallicity–redshift relation of Madau & Fragos (2017; Equation (A12)). Bottom left: we vary the threshold metallicity and the minimum time delay in a τ^{-1} time delay distribution. The inferred τ_{\min} is relatively independent of Z_{thresh} as long as $Z_{\text{thresh}} \gtrsim 0.2 Z_\odot$. Repeating the calculation with the mean metallicity–redshift relation of Langer & Norman (2006) yields similar results, with the resulting values for κ increasing by a nearly constant amount of ~ 0.3 across the parameter space. Bottom right: same as bottom left, but rather than a τ^{-1} time delay distribution, we assume a log-normal time delay distribution (Equation (3)) centered at μ with a width of 0.5 dex.

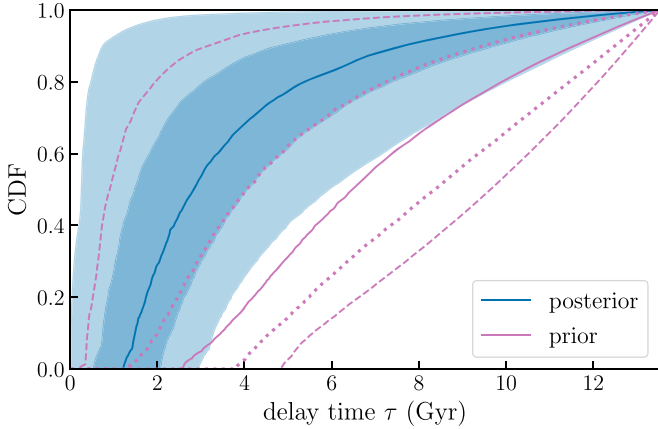


Figure 4. Inferred time delay distribution, shown as the cumulative distribution function (CDF) for a power-law model, assuming that the formation rate follows the SFR. Solid lines show the median CDF for the posterior (blue) and the prior (pink). Shaded blue bands enclose the central 50% and 90% of posterior CDFs at each delay time. The pink dotted (dashed) lines enclose 50% (90%) of the prior CDFs. Compared to the prior, the posterior favors short time delays.

evolution. Nevertheless, we can see from the bottom two panels of Figure 3 that the preference for small delay times $\tau \lesssim 3$ Gyr persists across all Z_{thresh} .

We can also repeat the analyses of the previous two subsections fixing the progenitor formation rate to the low-metallicity SFR with $Z < 0.3 Z_\odot$, rather than the total SFR; see the top right panel (“ $Z_{\text{thresh}} = 0.3 Z_\odot$ ”) of Figure 3. When we assumed that the progenitor formation followed the SFR with no metallicity dependence, we found that 43%–100% of systems experience delay times under 4.5 Gyr in the binned model and a median delay time of $\tau_{50\%} = 2.8^{+3.3}_{-2.6}$ Gyr in the power-law model. If we instead assume that the progenitor formation rate follows the low-metallicity SFR with $Z_{\text{thresh}} = 0.3 Z_\odot$ and repeat these analyses, we find that 37%–100% of systems experience delay times under 4.5 Gyr in the binned model, and that in the power-law model, the inferred median delay time is $\tau_{50\%} = 3.9^{+3.2}_{-3.5}$ Gyr. With an even stricter metallicity threshold of $Z_{\text{thresh}} = 0.1 Z_\odot$, the inferred median delay time is $\tau_{50\%} = 4.9^{+3.0}_{-4.3}$ Gyr. Within statistical uncertainties, the inferred time delay distributions are consistent across different values of Z_{thresh} , suggesting that the assumed metallicity threshold does not strongly impact the conclusions about the time delay distribution.

In addition to varying Z_{thresh} , we also explore how different assumptions about the metallicity scatter $\sigma_{\log Z}$ affect our inference about the time delay distribution. For a $p(\tau) \propto \tau^{-1}$ time delay distribution, we show the posterior on the minimum time delay for different values of Z_{thresh} and $\sigma_{\log Z}$ in Figure 5.

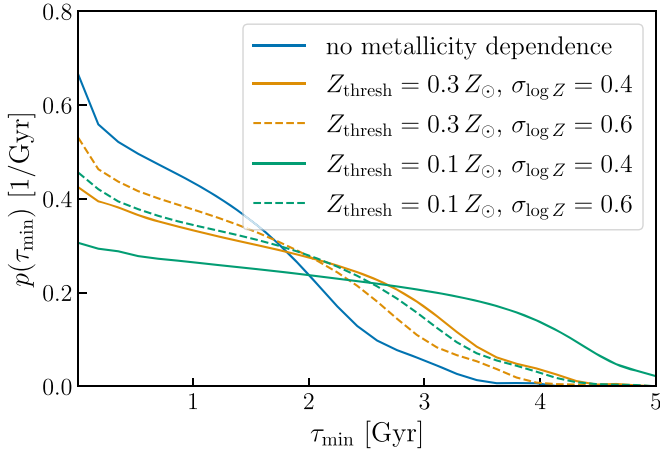


Figure 5. Posterior distribution of the minimum time delay τ_{\min} for a $p(\tau) \propto \tau^{-1}$ time delay distribution. The different lines correspond to different assumptions about the metallicity-dependence of the progenitor formation rate and the distribution of metallicities at a given redshift.

For all Z_{thresh} and $\sigma_{\log Z}$, we infer a preference for small time delays relative to our prior, with the posterior on τ_{\min} peaking at 10 Myr, the smallest time delay in our prior. Unsurprisingly, the preference for small time delays is strongest when we assume that the progenitor rate follows the total SFR without any metallicity dependence. Under this assumption, we find $\tau_{\min} < 2.2$ Gyr (90% upper limit). For $\sigma_{\log Z} = 0.4$ dex, we find $\tau_{\min} < 3.0$ Gyr for $Z_{\text{thresh}} = 0.3 Z_{\odot}$ and $\tau_{\min} < 3.8$ Gyr for $Z_{\text{thresh}} = 0.1 Z_{\odot}$, following the trends seen in the bottom left panel of Figure 3. When we assume that the metallicity distribution at each redshift is relatively broad ($\sigma_{\log Z} = 0.6$ dex), shown by the dashed lines of Figure 5, the inferred time delay distribution is less sensitive to Z_{thresh} , with $\tau_{\min} < 2.9$ Gyr even for the strictest metallicity threshold that we consider, $Z_{\text{thresh}} = 0.1 Z_{\odot}$.

Although we use the mean metallicity–redshift relation of Equation (A12) from Madau & Fragos (2017) throughout this subsection, adopting a different mean metallicity–redshift relation does not significantly affect the conclusions compared to current GW uncertainties on the inferred merger rate. For example, if we instead adopt the mean metallicity–redshift relation from Langer & Norman (2006), the values for the merger rate evolution slope κ in the bottom left panel of Figure 3 increase by a nearly uniform amount of ~ 0.3 across the plotted values of τ_{\min} and Z_{thresh} .

3.4. Effect of Black Hole Mass

In the previous subsections, we have assumed that the BBH merger rate evolves with redshift independently of mass, so that if we consider the merger rate within different BBH mass bins, the ratio of the merger rate at $z = 1$ to $z = 0$, $\mathcal{R}_1/\mathcal{R}_0$, is the same at all masses (shown by the blue band of Figure 6). This assumption is supported by population analyses of GWTC-2, which do not find strong evidence that the BBH mass distribution evolves with redshift (Fishbach et al. 2021). Nevertheless, BBH systems may experience different evolutionary processes, including different metallicity dependences and time delays, based on their masses. In fact, BBH systems in different mass ranges might be produced by different formation channels entirely (Zevin et al. 2021).

Fitting a population model that allows the mass distribution to evolve with redshift, Fishbach et al. (2021) found a mild

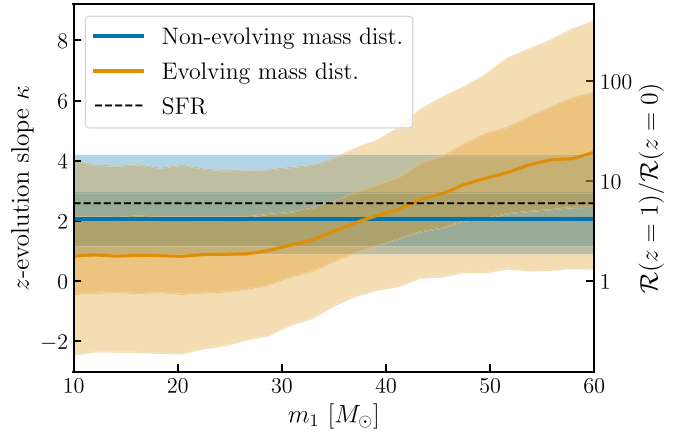


Figure 6. Inferred ratio of the merger rate at $z = 1$ to $z = 0$, or approximate power-law slope $\kappa = \frac{\ln(\mathcal{R}_1/\mathcal{R}_0)}{\ln 2}$, for BBH systems of a given primary mass. The blue band corresponds to the model of Section 2 in which the mass distribution is independent of redshift. The orange band corresponds to a model in which the mass distribution can evolve with redshift, from Fishbach et al. (2021). Solid lines denote medians and shaded bands denote central 50% and 90% credible intervals. The dashed black line shows the rate evolution of the SFR.

preference that the rate increases more steeply from $z = 0$ to $z = 1$ for heavier BBH systems compared to lighter systems. The orange band of Figure 6 shows $\kappa = \frac{\ln(\mathcal{R}_1/\mathcal{R}_0)}{\ln 2}$ as a function of primary mass, inferred using the evolving broken power-law model of Fishbach et al. (2021). We can use these results to infer different time delay distributions and/or progenitor formation rates as a function of BBH mass.

If we assume that the progenitor formation rate follows the same SFR across all masses but different time delay distributions, the high-mass ($m_1 \sim 50 M_{\odot}$) BBH systems exhibit a marginally stronger preference for small time delays than the low mass ($m_1 \sim 15 M_{\odot}$) BBH systems. Fitting for the minimum time delay in a τ^{-1} distribution, we find $\tau_{\min} < 3.2$ Gyr for BBH systems with $m_1 = 15 M_{\odot}$ and $\tau_{\min} < 2.4$ Gyr for BBH systems with $m_1 = 50 M_{\odot}$ (90% upper limits); in other words, the two posteriors are completely consistent with one another.

Alternatively, it is possible, although not required by the data, that the progenitor formation rate of the high-mass BBH systems peaks at earlier redshifts, perhaps because of a stricter requirement for low metallicities. However, at all threshold metallicities $Z_{\text{thresh}} \geq 0.1 Z_{\odot}$, in order for the merger rate to evolve faster than $\kappa \sim 2$, we require time delay distributions that are steeper than $\alpha_{\tau} = -1$ according to the bottom left panel of Figure 3. We also note that high-mass BBH mergers may be hierarchical merger products of lower mass BBHs, which would create a complicated dependence of the merger rate evolution between different mass bins (see Gerosa & Fishbach 2021 for a review).

4. Progenitor Formation Rate

While in the previous section we fixed the progenitor formation rate and extracted the time delay distribution, in this section we consider the reverse problem and extract the progenitor formation rate for a fixed time delay distribution. We use the SFR of Equation (A11) and the mean metallicity–redshift relation of Equation (A12) (Madau & Fragos 2017), and fit for the threshold metallicity Z_{thresh} , the scatter around the mean metallicity–redshift relation $\sigma_{\log Z}$, and the normalization

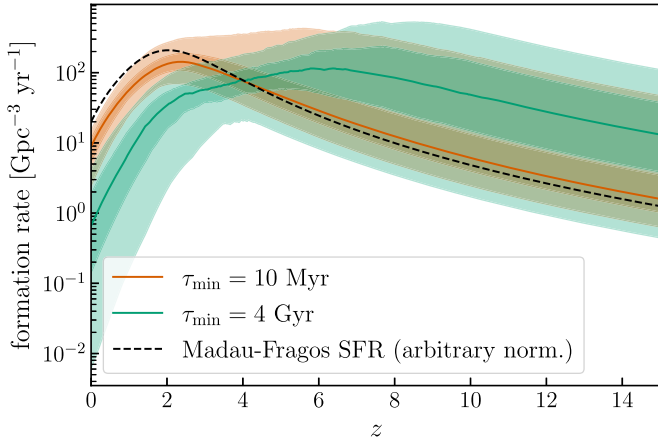


Figure 7. Inferred progenitor formation rate for a fixed power-law time delay model with $\alpha_\tau = -1$. We consider two different minimum delay times: $\tau_{\min} = 10$ Myr (orange) and $\tau_{\min} = 4$ Gyr (green). The progenitor formation rate is assumed to follow the low-metallicity SFR where we fit for the threshold metallicity, the scatter around the mean metallicity relation, and the formation efficiency. Solid lines show medians and shaded bands show central 50% and 90% credible regions. For reference, the dashed black line shows the Madau-Fragos SFR (Equation (A11)) with an arbitrary normalization.

$R_{f,0}$. The inferred progenitor formation rates for two different τ^{-1} time delay models are shown in Figure 7. We find that a time delay distribution that favors long time delays ($\tau_{\min} = 4$ Gyr) is possible only if the progenitor rate peaks at $z > 3.9$, or $t_L > 12$ Gyr (90% credibility, reweighting to a flat prior on the peak redshift in the range 2.1–9.). This result is driven by the absence of a peak in the BBH merger rate density at $z < 1$ ($t_L \lesssim 8$ Gyr), so that for any minimum delay time τ_{\min} , the progenitor formation rate probably peaked at a lookback time $t_L > \tau_{\min} + 8$ Gyr. A time delay distribution with $\tau_{\min} = 4$ Gyr requires a strict metallicity threshold, favoring the lowest metallicity threshold in our prior ($Z_{\text{thresh}} = 0.1 Z_\odot$) by a Bayes factor of 40 compared to no metallicity weighting; see also the bottom left panel of Figure 3.

Meanwhile, for a time delay distribution that favors short time delays ($\tau_{\min} = 10$ Myr), as predicted for the isolated binary evolution channel (O’Shaughnessy et al. 2010; Dominik et al. 2012; Mapelli et al. 2017; Neijssel et al. 2019), we infer a progenitor formation rate that matches the SFR well, but also permits the peak formation rate to occur at higher redshifts. Assuming the short-time delay model, the data remain uninformative about the metallicity dependence, with our posterior over Z_{thresh} recovering the prior. Also interesting to note is that the inferred amplitude of the progenitor formation rate at $z = 0$, $R_{f,0}$, related to the BBH formation efficiency, differs for the two time delay models, with $R_{f,0} = 7.8^{+3.65}_{-5.0}$ $\text{Gpc}^{-3} \text{yr}^{-1}$ for the $\tau_{\min} = 4$ Gyr model and $R_{f,0} = 7.8^{+8.3}_{-5.0}$ $\text{Gpc}^{-3} \text{yr}^{-1}$ for the $\tau_{\min} = 10$ Myr model.

5. Conclusion

We have derived the first observational constraints on the BBH time delay distribution and the formation rate of their progenitors from the latest LIGO-Virgo catalog, GWTC-2. We found that with only 44 BBH events out to $z \lesssim 1$, we can already rule out models in which time delays are longer than ~ 3 Gyr if the progenitor formation rate is close to the SFR. Our main results are as follows:

1. Short time delays are favored for all progenitor formation rates we consider. For a progenitor formation rate that follows the SFR, we find that 43%–100% of mergers have time delays $\tau < 4.5$ Gyr. For a $p(\tau) \propto \tau^{-1}$ time delay distribution, we find that the time delay distribution peaks below $\tau_{\min} < 2.2$ Gyr if the progenitor formation rate follows the SFR. This corresponds to median time delays $\tau_{50\%} = 2.8^{+3.3}_{-2.6}$ Gyr. If the progenitor formation rate follows the low-metallicity ($Z < 0.3 Z_\odot$) SFR, we find $\tau_{\min} < 3.0$ Gyr, with $\tau_{50\%} = 3.9^{+3.2}_{-3.5}$ Gyr.
2. If the time delay distribution favors longer delay times ($\tau \gtrsim 4$ Gyr), the progenitor formation rate must peak earlier than the SFR. For example, for a τ^{-1} time delay distribution with $\tau_{\min} = 4$ Gyr, the progenitor formation rate peaks at $z > 3.9$, and is fairly low at $z = 0$, with $R_{f,0} = 0.74^{+3.65}_{-0.73}$ $\text{Gpc}^{-3} \text{yr}^{-1}$. If the progenitor formation rate is related to the SFR, this requires that the progenitors only form at low metallicities $Z < 0.1 Z_\odot$. On the other hand, if we assume a τ^{-1} time delay distribution with $\tau_{\min} = 10$ Myr, motivated by predictions from isolated binary evolution, we constrain the progenitor formation rate at $z = 0$ to be $R_{f,0} = 7.8^{+8.3}_{-5.0}$ $\text{Gpc}^{-3} \text{yr}^{-1}$. The shape of the progenitor formation rate matches the SFR well.
3. There is no strong evidence that the time delay distribution or the progenitor formation rate varies with mass. However, it is possible that more massive systems experience shorter delay times and/or a stricter low-metallicity threshold.

We can use the constraints on the time delay distribution to probe the evolutionary pathways that give rise to BBH systems, with the caveat that our analysis only applies to formation channels in which BBH progenitors follow the (low-metallicity) star formation rate. Thus, our measurement of the time delay distribution does not directly apply to primordial BH channels (see Sasaki et al. 2018 for a review), BBH mergers in AGN disks, and dynamical assembly in globular clusters if they were predominantly formed during the reionization epoch, rather than concurrently with star formation (Forbes et al. 2018; Romero-Shaw et al. 2020).

With the current GW catalog, the inferred time delay distribution remains consistent with most of the formation channels discussed in Section 1. There may be hints of tension with formation scenarios that favor longer time delays, like stellar triples (where most time delays are greater than ~ 1 Gyr, and BBH formation is expected to be relatively efficient at high metallicities), and chemically homogeneous binaries (where most time delays are greater than a few gigayears, but the low-metallicity requirement for BBH formation may be much stricter).

Nevertheless, we can see from Figure 3 how our constraints on the time delay distribution and the progenitor metallicity dependence will improve as the measurement of the redshift evolution slope κ tightens. At O3 sensitivity, the width of the 90% credible interval on κ converges with the number of events N as $\Delta_{90\%}(\kappa) \sim 31/\sqrt{N}$ (Fishbach et al. 2018); this is well matched by the current measurement $\Delta_{90\%}(\kappa) = 4.3$ with ~ 50 events. With more sensitive detectors, the measurement of κ is expected to converge faster; $\Delta_{90\%}(\kappa)$ scales inversely with the average $\ln(1+z)$ among detected events. For detectors that are 50% more sensitive, as expected for Advanced LIGO at design sensitivity, it is likely that 500 events (around a year of

observation) will constrain κ to $\Delta_{90\%}(\kappa) = 1$. If the inferred merger rate prefers relatively steep evolution ($\kappa \gtrsim 2$), this will put pressure on many time delay models, requiring time delay distributions that are steeper than flat-in-log and/or a strict low-metallicity requirement for progenitor formation (see Figure 3). In addition to inferring the time delay distribution and the BBH formation efficiency as a function of metallicity, the BBH merger rate can yield insight into the metallicity evolution of the universe. Another exciting application of this calculation would be to determine which time delay model (for example, power law versus log-normal) best fits the data, which would reveal details of the BBH formation model. The binned time delay model of Section 3.1 has the advantage of naturally incorporating all possible models via its flexibility, although meaningful model selection will likely only be possible once the peak of the merger rate is resolved, either with continued observation of the stochastic background (Callister et al. 2020) or with the next generation of ground-based GW detectors (Vitale et al. 2019).

M.F. is supported by NASA through NASA Hubble Fellowship grant HST-HF2-51455.001-A awarded by the Space Telescope Science Institute. V.K. is supported by a CIFAR G +EU Senior Fellowship and Northwestern University. This research has made use of GWTC-2 parameter estimation samples obtained from the Gravitational Wave Open Science Center (<https://www.gw-openscience.org/>), a service of LIGO Laboratory, the LIGO Scientific Collaboration and the Virgo Collaboration. LIGO Laboratory and Advanced LIGO are funded by the United States National Science Foundation (NSF) as well as the Science and Technology Facilities Council (STFC) of the United Kingdom, the Max-Planck-Society (MPS), and the State of Niedersachsen/Germany for support of the construction of Advanced LIGO and construction and operation of the GEO600 detector. Additional support for Advanced LIGO was provided by the Australian Research Council. Virgo is funded, through the European Gravitational Observatory (EGO), by the French Centre National de Recherche Scientifique (CNRS), the Italian Istituto Nazionale di Fisica Nucleare (INFN) and the Dutch Nikhef, with contributions by institutions from Belgium, Germany, Greece, Hungary, Ireland, Japan, Monaco, Poland, Portugal, Spain. This document has been assigned LIGO document number P2100164.

Software: ASTROPY (Astropy Collaboration et al. 2018), EMCEE (Foreman-Mackey et al. 2013), NUMPY (Harris et al. 2020), MATPLOTLIB (Hunter 2007), PESUMMARY (Hoy & Raymond 2020), PYMC3 (Salvatier et al. 2016), SCIPY (Virtanen et al. 2020), SEABORN (Waskom et al. 2020), THEANO (The Theano Development Team et al. 2016).

Appendix Statistical Framework

We write the differential number density of BBH systems as:

$$\frac{d\mathcal{N}}{dm_1 dm_2 d\chi_{\text{eff}} dz dt_d} \equiv N p(m_1, m_2, \chi_{\text{eff}}, z), \quad (\text{A1})$$

where m_1 and m_2 are the primary and secondary component masses, χ_{eff} is the effective inspiral spin, z is the source redshift, t_d is time measured in the detector-frame, p is a normalized probability density that integrates to unity over the considered range of masses, spins, and redshifts, and N is the

number of BBHs within the mass, spin, and redshift range that merge during the observing time $T_{\text{obs}} = \int dt_d$. We are primarily concerned with the redshift distribution in this work, but the inferred redshift distribution correlates with the inferred mass and, to a lesser extent, χ_{eff} distribution, and so we must consider these properties jointly. The merger rate density is:

$$\begin{aligned} \mathcal{R}(z) &\equiv \frac{d\mathcal{N}}{dV_c dt_s} = \frac{d\mathcal{N}}{dz dt_d} \left(\frac{dV_c}{dz} \right)^{-1} \frac{dt_d}{dt_s} \\ &= \frac{d\mathcal{N}}{dz} \left(\frac{dV_c}{dz} \right)^{-1} \frac{T_{\text{obs}}}{1+z}, \end{aligned} \quad (\text{A2})$$

where:

$$\frac{d\mathcal{N}}{dz} \equiv N \int p(m_1, m_2, \chi_{\text{eff}}, z) dm_1 dm_2 d\chi_{\text{eff}}. \quad (\text{A3})$$

We adopt a parameterized model to describe the population distribution $p(m_1, m_2, \chi_{\text{eff}}, z|\lambda)$, where λ are the parameters of the model. For now, we assume that the mass and spin distributions are independent of redshift, so that:

$$\begin{aligned} p(m_1, m_2, \chi_{\text{eff}}, z|\lambda) &= p(m_1, m_2|\lambda_m) p \\ &\times (\chi_{\text{eff}}|\lambda_\chi) p(z|\lambda_z), \end{aligned} \quad (\text{A4})$$

and:

$$\mathcal{R}(z) = N p(z) \left(\frac{dV_c}{dz} \right)^{-1} \frac{T_{\text{obs}}}{1+z}. \quad (\text{A5})$$

We use the BROKEN POWER LAW mass model from Abbott et al. (2021b) to describe $p(m_1, m_2|\lambda_m)$ and the GAUSSIAN spin model from Miller et al. (2020) and Abbott et al. (2021b) to describe $p(\chi_{\text{eff}}|\lambda_\chi)$. The primary mass distribution follows a power law with slope α_1 between m_{min} and m_{break} and slope α_2 between m_{break} and m_{max} . The mass ratio distribution follows a power law with slope β_q . The χ_{eff} distribution is described by a Gaussian with mean $\mu_{\chi_{\text{eff}}}$ and standard deviation $\sigma_{\chi_{\text{eff}}}$, truncated to the physical range $-1 < \chi_{\text{eff}} < 1$ (Roulet & Zaldarriaga 2019; Miller et al. 2020). For the redshift evolution model $p(z|\lambda_z)$, we write:

$$p(z|\lambda_z) \propto \frac{dV_c}{dz} \frac{1}{1+z} f(z|\lambda_z). \quad (\text{A6})$$

For $f(z)$, we include the possibility that the merger rate peaks at a redshift $z < 1$ by using a smoothly broken power law in $(1+z)$, where (Astropy Collaboration et al. 2018):

$$f(z|\kappa, \gamma, z_p, \Delta) = \left(\frac{1+z}{1+z_p} \right)^\kappa \left[\frac{1 + \left(\frac{1+z}{1+z_p} \right)^{1/\Delta}}{2} \right]^{(\gamma-\kappa)\Delta}, \quad (\text{A7})$$

and we fix the smoothing parameter $\Delta = 0.2$. This model with $\kappa = 2.6$, $\gamma = -3.6$, $z_p = 2.2$, and $\Delta = 0.16$ can reproduce the shape of the Madau & Fragos (2017) SFR. We note that with the current data, we cannot observe the peak redshift z_p , but can rule out that the merger rate peaks at $z \lesssim 1$.

We fit for the population parameters λ with the usual hierarchical Bayesian framework (Mandel 2010; Farr 2019; Mandel et al. 2019), using the same parameter estimation samples and detector sensitivity estimate as

Table 1
Summary of Population Hyperparameters λ in Equation (A4)

Parameter	Description	Prior
m_{\min}/M_{\odot}	Minimum BH mass	U(2, 10)
$m_{\text{break}}/M_{\odot}$	Mass at which the power law describing the primary mass distribution breaks	U(20, 65)
m_{\max}/M_{\odot}	Maximum BH mass	U(65, 100)
α_1	Power-law slope of the primary mass distribution for masses below m_{break}	U(-5, 2)
α_2	Power-law slope of the primary mass distribution for masses above m_{break}	U(-12, 2)
β_q	Power-law slope of the mass ratio distribution	U(-4, 12)
$\mu_{\chi_{\text{eff}}}$	Mean of the Gaussian describing the χ_{eff} distribution	U (-0.5, 0.5)
$\sigma_{\chi_{\text{eff}}}$	Standard deviation of the Gaussian describing the χ_{eff} distribution	U(0.02, 1)
z_p	Redshift at which the merger rate peaks	U(0, 3)
κ	Power-law slope in $(1+z)$ of the merger rate evolution for $z < z_p$	U(0, 6)
γ	Power-law slope in $(1+z)$ of the merger rate evolution for $z > z_p$	U(-6, 0)

Note. We organize the hyperparameters into three groups: the mass distribution parameters λ_m , the spin distribution parameters λ_χ , and the redshift distribution parameters λ_z . The notation U(a , b) denotes a uniform distribution between a and b .

Abbott et al. (2021b). We take broad, flat priors on all parameters λ as detailed in Table 1, and a flat-in-log prior on the normalization parameter N . We sample from the posterior over the model parameters λ with PyMC3 (Salvatier et al. 2016).

Our goal is to extract information about the delay time distribution and the progenitor formation rate from this inferred merger rate evolution. Given the progenitor formation rate R_f and a time delay distribution $p(\tau)$, we can calculate the resulting merger rate as a function of lookback time:

$$\mathcal{R}(t_L) = \int_{\tau_{\min}}^{\tau_{\max}} R_f(t_L + \tau) p(\tau) d\tau, \quad (\text{A8})$$

where t_L is the lookback time corresponding to merger and $t_L + \tau$ is the lookback time corresponding to formation for a given time delay τ . Under an assumed cosmological model, the lookback time can be calculated from the redshift z . We use the median *Planck 2015* cosmological parameters (Planck Collaboration et al. 2016). Throughout this work, we assume the earliest progenitor formation time was 13.5 Gyr ago, corresponding to a maximum formation redshift $z = 14$, so we fix $\tau_{\max} = 13.5$ Gyr to restrict to systems that have already merged.

If we have a binned time delay distribution, as in Equation (1),

$$p(\tau) = \sum_{i=1}^n p_i \Theta(b_i \leq \tau < b_{i+1}), \quad (\text{A9})$$

it is straightforward to compute the merger rate of Equation (A8):

$$\mathcal{R}(t_L) = \sum_{i=1}^n p_i (F(t_L + b_{i+1}) - F(t_L + b_i)), \quad (\text{A10})$$

where F is the integral of the formation rate as a function of lookback time, $F(x) = \int_0^x R_f(t_L) dt_L$. We convert lookback time to redshift, $z(t_L)$, to write Equation (A10) in terms of $\mathcal{R}(z)$.

We assume that the progenitor formation rate R_f depends on the SFR, as reported in Madau & Fragos (2017):

$$R_{\text{SFR}}(z) \propto \frac{(1+z)^{2.6}}{1 + \left(\frac{1+z}{3.2}\right)^{6.2}}. \quad (\text{A11})$$

We also consider models in which the formation rate of BBH progenitors does not follow the total SFR, but rather follows only the low-metallicity SFR below some threshold metallicity Z_{thresh} . This assumption is equivalent to a model in which the BBH formation efficiency depends on metallicity, and this metallicity dependence can be approximated by a step function: the efficiency is constant for $Z \leq Z_{\text{thresh}}$ and sharply turns off at $Z > Z_{\text{thresh}}$. When considering the low-metallicity SFR, we adopt the mean metallicity–redshift relation from Madau & Fragos (2017):

$$\langle \log_{10} Z(z)/Z_{\odot} \rangle = 0.153 - 0.074z^{1.34}. \quad (\text{A12})$$

The distribution of metallicities at each redshift, particularly the scatter, is uncertain (Chruslinska et al. 2019). We assume that $\log_{10} Z(z)$ follows a normal distribution at each z with some standard deviation $\sigma_{\log Z}$. We adopt the default value of $\sigma_{\log Z} = 0.4$ dex, as in Neijssel et al. (2019) and Bouffanais et al. (2021), although we sometimes treat it as a free parameter in the model.

For the binned time delay model, we substitute $\mathcal{R}(z)$ as calculated in Equation (A10) for $f(z|\lambda_z)$ in Equation (A6), and jointly fit λ_m , λ_χ , and the time delay bin heights p_i , as described in Section 3.1 of the main text. See Tables 1 and 2 for the sampling priors on the hyperparameters. When fitting the other time delay and progenitor formation rate models, we approximate the full hierarchical Bayesian likelihood as follows.

We observe that the joint posterior for \mathcal{R}_1 and \mathcal{R}_0 is insensitive to the assumed parameterization of the redshift distribution, whether we fit a one-parameter power law in $(1+z)$, the smoothly broken power-law model of Equation (A7), or the physical, binned time delay model of the previous Section 3.1. The marginal one-dimensional posteriors are $\mathcal{R}_0 = 18_{-9}^{+17}$ Gpc $^{-3}$ yr $^{-1}$ and $\mathcal{R}_1 = 66_{-46}^{+190}$ Gpc $^{-3}$ yr $^{-1}$. This observation allows us to speed up the inference by approximating the likelihood of the GW catalog given the time delay distribution as follows. We are interested in fitting for the parameters specifying the time delay distribution—for example, a power law with slope α_τ and minimum delay τ_{\min} —together with the parameters specifying the formation rate: the metallicity threshold Z_{thresh} , the scatter about the mean–metallicity relation $\sigma_{\log Z}$, and the amplitude of the formation rate $R_f(0) = R_{f,0}$ (equivalently, the BBH formation efficiency). Denoting these parameters by $\theta \equiv \{\alpha_\tau, \tau_{\min}, Z_{\text{thresh}}, \sigma_{\log Z}, R_{f,0}\}$, we calculate $\mathcal{R}_1(\theta)$ and $\mathcal{R}_0(\theta)$ by Equation (A8) as in Figure 3. We are interested in the posterior probability distribution of θ given the GW data, d :

$$p(\theta|d) \propto p(d|\theta) p_0(\theta), \quad (\text{A13})$$

where p_0 represents the prior probability and we approximate the likelihood:

$$p(d|\theta) \approx p(d|\mathcal{R}_1(\theta), \mathcal{R}_0(\theta)). \quad (\text{A14})$$

Table 2
Summary of Hyperparameters Describing the Time Delay Distribution and the Progenitor Formation Rate

Parameter	Description	Prior
$\{p_i(b_{i+1} - b_i)\}_{i=1,2,3}$	Fraction of systems with delay times between b_i and b_{i+1} in the binned time delay model	Dir(0.5, 0.5, 0.5)
τ_{\min}/Gyr	Minimum time delay in the power-law time delay model	U(0.01, 5)
α_τ	Power-law slope of the time delay distribution in the power-law model	U(-3, 1)
$R_{f,0}/\text{Gpc}^{-3}\text{yr}^{-1}$	Progenitor formation rate at $z = 0$	LU(10^{-3} , 100)
$Z_{\text{thresh}}/Z_\odot$	Threshold metallicity for progenitor formation	U(0.1, 2)
$\sigma_{\log Z}$	Scatter about the mean metallicity–redshift relation	U(0.2, 0.6)

Note. The notation Dir($\alpha_1, \dots, \alpha_k$) denotes a Dirichlet distribution with concentration parameters α_i , $U(a, b)$ a uniform distribution between a and b , and LU(a, b) a log-uniform distribution, so that $X \sim \text{LU}(a, b)$ implies $\log X \sim U(\log a, \log b)$.

We calculate $p(d|\mathcal{R}_1, \mathcal{R}_0)$ from the phenomenological population fit of Section 2, where we computed the likelihood given the population parameters $p(d|N, \lambda_m, \lambda_\chi, \lambda_z)$. From the population parameters N (one-dimensional) and λ_z (three-dimensional), we calculate $\mathcal{R}_0(N, \lambda_z)$ and $\mathcal{R}_1(N, \lambda_z)$ according to Equation (A2). Given (N, λ) posterior samples drawn from:

$$p(N, \lambda|d) \propto p(d|N, \lambda)p_0(N, \lambda), \quad (\text{A15})$$

where $\lambda \equiv \{\lambda_m, \lambda_\chi, \lambda_z\}$, we apply the function $\mathcal{R}(z, \lambda_z, N)$ at $z = 0$ and $z = 1$ to get samples from the probability density $p(\mathcal{R}_0, \mathcal{R}_1|d)$. We then also draw prior samples (N, λ) drawn from $p_0(N, \lambda)$ to calculate $p_0(\mathcal{R}_0, \mathcal{R}_1)$. Given these two sets of posterior and prior samples, we approximate both the posterior density and the prior density with a Gaussian kernel density estimate to evaluate the approximate likelihood:

$$p(d|\mathcal{R}_0, \mathcal{R}_1) \propto \frac{p(\mathcal{R}_0, \mathcal{R}_1|d)}{p_0(\mathcal{R}_0, \mathcal{R}_1)}, \quad (\text{A16})$$

which we can substitute into the desired posterior probability distribution for θ through Equations (A13) and (A14). For $p_\theta(\theta)$, our default priors are shown in Table 2.

ORCID iDs

Maya Fishbach  <https://orcid.org/0000-0002-1980-5293>
Vicky Kalogera  <https://orcid.org/0000-0001-9236-5469>

References

Abbott, B. P., Abbott, R., Abbott, T. D., et al. 2019, *ApJL*, **882**, L24
 Abbott, R., Abbott, T. D., Abraham, S., et al. 2021a, *PhRvX*, **11**, 021053
 Abbott, R., Abbott, T. D., Abraham, S., et al. 2021b, *ApJL*, **913**, L7
 Abbott, R., Abbott, T. D., Abraham, S., et al. 2021c, arXiv:2101.12130
 Abt, H. A. 1983, *ARA&A*, **21**, 343
 Acernese, F., Agathos, M., Agatsuma, K., et al. 2015, *CQGra*, **32**, 024001
 Antonini, F., Toonen, S., & Hamers, A. S. 2017, *ApJ*, **841**, 77
 Astropy Collaboration, Price-Whelan, A. M., Sipőcz, B. M., et al. 2018, *AJ*, **156**, 123
 Banerjee, S. 2017, *MNRAS*, **467**, 524
 Banerjee, S. 2021, *MNRAS*, **503**, 3371
 Banerjee, S., Baumgardt, H., & Kroupa, P. 2010, *MNRAS*, **402**, 371
 Belczynski, K., Dominik, M., Bulik, T., et al. 2010, *ApJL*, **715**, L138
 Belczynski, K., Holz, D. E., Bulik, T., & O’Shaughnessy, R. 2016, *Natur*, **534**, 512
 Benacquista, M. J., & Downing, J. M. B. 2013, *LRR*, **16**, 4
 Bouffanais, Y., Mapelli, M., Santoliquido, F., et al. 2021, arXiv:2102.12495
 Brott, I., de Mink, S. E., Cantiello, M., et al. 2011, *A&A*, **530**, A115
 Callister, T., Fishbach, M., Holz, D. E., & Farr, W. M. 2020, *ApJL*, **896**, L32
 Chruslińska, M., Jeřábková, T., Nelemans, G., & Yan, Z. 2020, *A&A*, **636**, A10
 Chruslińska, M., & Nelemans, G. 2019, *MNRAS*, **488**, 5300
 Chruslińska, M., Nelemans, G., & Belczynski, K. 2019, *MNRAS*, **482**, 5012

Di Carlo, U. N., Mapelli, M., Giacobbo, N., et al. 2020, *MNRAS*, **498**, 495
 Dominik, M., Belczynski, K., Fryer, C., et al. 2012, *ApJ*, **759**, 52
 Dominik, M., Belczynski, K., Fryer, C., et al. 2013, *ApJ*, **779**, 72
 du Buisson, L., Marchant, P., Podsiadlowski, P., et al. 2020, *MNRAS*, **499**, 5941
 El-Badry, K., Quataert, E., Weisz, D. R., Choksi, N., & Boylan-Kolchin, M. 2019, *MNRAS*, **482**, 4528
 Elbert, O. D., Bullock, J. S., & Kaplinghat, M. 2018, *MNRAS*, **473**, 1186
 Farr, W. M. 2019, *RNAAS*, **3**, 66
 Fishbach, M., Doctor, Z., Callister, T., et al. 2021, arXiv:2101.07699
 Fishbach, M., Holz, D. E., & Farr, W. M. 2018, *ApJL*, **863**, L41
 Forbes, D. A., Bastian, N., Gieles, M., et al. 2018, *RSPSA*, **474**, 20170616
 Foreman-Mackey, D., Conley, A., Meierjürgen Farr, W., et al. 2013, emcee: The MCMC Hammer, Astrophysics Source Code Library, ascl:1303.002
 Fragione, G., & Kocsis, B. 2018, *PhRvL*, **121**, 161103
 Fryer, C. L., Belczynski, K., Wiktorowicz, G., et al. 2012, *ApJ*, **749**, 91
 Gerosa, D., & Fishbach, M. 2021, arXiv:2105.03439
 Harris, C. R., Millman, K. J., van der Walt, S. J., et al. 2020, *Natur*, **585**, 357
 Hoang, B.-M., Naoz, S., Kocsis, B., Rasio, F. A., & Dosopoulou, F. 2018, *ApJ*, **856**, 140
 Hoy, C., & Raymond, V. 2020, arXiv:2006.06639
 Hunter, J. D. 2007, *CSE*, **9**, 90
 Kalogera, V., Berry, C. P. L., Colpi, M., et al. 2019, *BAAS*, **51**, 242
 Kremer, K., Ye, C. S., Rui, N. Z., et al. 2020, *ApJS*, **247**, 48
 Kruckow, M. U., Tauris, T. M., Langer, N., Kramer, M., & Izzard, R. G. 2018, *MNRAS*, **481**, 1908
 Kudritzki, R.-P., & Puls, J. 2000, *ARA&A*, **38**, 613
 Lamberts, A., Garrison-Kimmel, S., Clausen, D. R., & Hopkins, P. F. 2016, *MNRAS*, **463**, L31
 Langer, N., & Norman, C. A. 2006, *ApJL*, **638**, L63
 LIGO Scientific Collaboration, Aasi, J., Abbott, B. P., et al. 2015, *CQGra*, **32**, 074001
 Ma, X., Kasen, D., Hopkins, P. F., et al. 2015, *MNRAS*, **453**, 960
 Madau, P., & Dickinson, M. 2014, *ARA&A*, **52**, 415
 Madau, P., & Fragos, T. 2017, *ApJ*, **840**, 39
 Mandel, I. 2010, *PhRvD*, **81**, 084029
 Mandel, I., & de Mink, S. E. 2016, *MNRAS*, **458**, 2634
 Mandel, I., Farr, W. M., & Gair, J. R. 2019, *MNRAS*, **486**, 1086
 Mapelli, M., Giacobbo, N., Ripamonti, E., & Spera, M. 2017, *MNRAS*, **472**, 2422
 Marchant, P., Langer, N., Podsiadlowski, P., Tauris, T. M., & Moriya, T. J. 2016, *A&A*, **588**, A50
 Miller, S., Callister, T. A., & Farr, W. M. 2020, *ApJ*, **895**, 128
 Neijssel, C. J., Vigna-Gómez, A., Stevenson, S., et al. 2019, *MNRAS*, **490**, 3740
 Ng, K. K. Y., Vitale, S., Farr, W. M., & Rodriguez, C. L. 2021, *ApJL*, **913**, L5
 O’Shaughnessy, R., Belczynski, K., & Kalogera, V. 2008, *ApJ*, **675**, 566
 O’Shaughnessy, R., Kalogera, V., & Belczynski, K. 2010, *ApJ*, **716**, 615
 Peters, P. C. 1964, *PhRv*, **136**, 1224
 Planck Collaboration, Ade, P. A. R., Aghanim, N., et al. 2016, *A&A*, **594**, A13
 Rodriguez, C. L., Amaro-Seoane, P., Chatterjee, S., & Rasio, F. A. 2018, *PhRvL*, **120**, 151101
 Rodriguez, C. L., & Antonini, F. 2018, *ApJ*, **863**, 7
 Rodriguez, C. L., Chatterjee, S., & Rasio, F. A. 2016, *PhRvD*, **93**, 084029
 Rodriguez, C. L., & Loeb, A. 2018, *ApJL*, **866**, L5
 Romero-Shaw, I. M., Kremer, K., Lasky, P. D., Thrane, E., & Samsing, J. 2020, arXiv:2011.14541
 Roulet, J., Venumadhav, T., Zackay, B., Dai, L., & Zaldarriaga, M. 2020, *PhRvD*, **102**, 123022
 Roulet, J., & Zaldarriaga, M. 2019, *MNRAS*, **484**, 4216

- Safarzadeh, M., Berger, E., Ng, K. K. Y., et al. 2019, *ApJL*, **878**, L13
- Safarzadeh, M., Biscoveanu, S., & Loeb, A. 2020, *ApJ*, **901**, 137
- Salvatier, J., Wiecki, T. V., & Fonnesbeck, C. 2016, PyMC3: Python probabilistic programming framework, Astrophysics Source Code Library, ascl:1610.016
- Samsing, J. 2018, *PhRvD*, **97**, 103014
- Sana, H., de Koter, A., de Mink, S. E., et al. 2013, *A&A*, **550**, A107
- Santoliquido, F., Mapelli, M., Bouffanais, Y., et al. 2020, *ApJ*, **898**, 152
- Santoliquido, F., Mapelli, M., Giacobbo, N., Bouffanais, Y., & Artale, M. C. 2021, *MNRAS*, **502**, 4877
- Sasaki, M., Suyama, T., Tanaka, T., & Yokoyama, S. 2018, *CQGra*, **35**, 063001
- Schafer, J. L. 1997, Analysis of Incomplete Multivariate Data (London: Chapman & Hall)
- Tang, P. N., Eldridge, J. J., Stanway, E. R., & Bray, J. C. 2020, *MNRAS*, **493**, L6
- The Theano Development Team, Al-Rfou, R., Alain, G., et al. 2016, arXiv:1605.02688
- Tiwari, V. 2020, arXiv:2012.08839
- Vangioni, E., Olive, K. A., Prestegard, T., et al. 2015, *MNRAS*, **447**, 2575
- Virtanen, P., Gommers, R., Burovski, E., et al. 2020, scipy/scipy: SciPy 1.5.3, v1.5.3, Zenodo, doi:10.5281/zenodo.4100507
- Vitale, S., Farr, W. M., Ng, K. K. Y., & Rodriguez, C. L. 2019, *ApJL*, **886**, L1
- Waskom, M., Botvinnik, O., Gelbart, M., et al. 2020, seaborn: Statistical data visualization, Astrophysics Source Code Library, ascl:2012.015
- Yang, Y., Bartos, I., Haiman, Z., et al. 2020, *ApJ*, **896**, 138
- Zevin, M., Bavera, S. S., Berry, C. P. L., et al. 2021, *ApJ*, **910**, 152